

Influences of lidar scanning parameters on wind turbine wake retrievals in complex terrain

Rachel Robey¹ and Julie K. Lundquist^{2,3,4}

¹Department of Applied Mathematics, University of Colorado Boulder, Boulder, Colorado, USA

²Department of Atmospheric and Oceanic Sciences, University of Colorado Boulder, Boulder, Colorado, USA

³Department of Earth and Planetary Sciences, Department of Mechanical Engineering, Johns Hopkins University, Baltimore, Maryland, USA

⁴National Renewable Energy Laboratory, Golden, Colorado, USA

Correspondence: Rachel Robey (rachel.robey@colorado.edu)

Abstract. Scanning lidars enable the collection of spatially distributed measurements of turbine wakes and the estimation of wake properties such as magnitude, extent, and trajectory. Lidar-based characterizations, however, may be subject to distortions due to the observational system. Distortions can arise from the resolution of the measurement points across the wake, the projection of the winds onto the beam, averaging along the beam probe volume, and intervening evolution of the flow over the scan duration. Using a large-eddy simulation and simulated measurements with a virtual lidar model, we assess how scanning lidar systems may influence the properties of the retrieved wake using a case study from the Perdigão campaign. We consider three lidars performing range-height indicator sweeps in complex terrain, based on the deployments of lidars from the Danish Technical University (DTU) and German Aerospace Center (DLR) at the Perdigão site. The unwaked flow, measured by the DTU lidar, is well-captured by the lidar, even without combining data into a multi-lidar retrieval. The two DLR lidars measure a waked transect from different downwind vantage points. In the region of the wake, the observation system reacts to the smaller spatial and temporal variations of the winds, allowing more significant observation distortions to arise. While the measurements largely capture the wake structure and trajectory over its 4-5 D extent, limited spatial resolution of measurement points and volume averaging lead to a quicker loss of the two-lobes in the near wake, smearing of the vertical bounds of the wake (<30 m), wake center displacements up to 10 m, and dampening of the maximum velocity deficit by up to a third. The virtual lidar tool, coupled with simulations, provides a means for assessing measurements capabilities in advance of measurement campaigns.

1 Introduction

Scanning lidars are increasingly employed in the collection of spatially distributed measurements of wind turbine wakes (Menke et al., 2019; Bodini et al., 2017; Moriarty et al., 2020), which are characterized by reduced wind speeds and increased turbulence. Lidar measurements may be used to diagnose key metrics such as the magnitude of the velocity deficit, the spatial extent of the wake, and the trajectory followed by the wake. Building from promising early deployments for wake measurements in the early 2000s (Käsler et al., 2010), scanning lidars have become a staple in many field campaigns for assessing wind turbine wakes (Aitken et al., 2014; Aitken and Lundquist, 2014; Barthelmie and Pryor, 2019; Bodini et al., 2017;

Brugger et al., 2020; Gottschall, 2020; Iungo et al., 2013; Menke et al., 2018; Smalikho et al., 2013; Wildmann et al., 2018b) and other complex flow features like recirculation zones (Menke et al., 2019) or urban flow features (Newsom et al., 2008).

25 Investigations of turbine wakes with lidar were initially conducted in fairly simple terrain (e.g. Käsler et al. (2010); Aitken et al. (2014); Bodini et al. (2017)). For a detailed summary of lidar measurements of wakes, see Gottschall (2020). More recent studies have explored the variability of wakes in complex terrain. The Perdigão field campaign (Fernando et al., 2019) was a seminal study at a site featuring parallel double ridges and a single 2 MW turbine, the wake of which was captured through an extensive array of scanning lidar (Fig. 1). The wake behavior in the highly complex site using the lidar data and different
30 scanning strategies are explored in Wildmann et al. (2018b), Menke et al. (2018), and Barthelmie and Pryor (2019).

Wake characterizations based on lidar data, however, may be subject to distortions due to inherent properties of the observational system. Even assuming perfect calibration and sufficient air quality to ensure adequate backscatter signals, the measurements are subject to the spatial resolution of retrieval points, projection of the winds onto the lidar beam, averaging along the beam probe volume, and intervening evolution of the flow over the scan duration. Possible measurement and scan
35 techniques have grown in complexity in part to address some of these issues, e.g., combining multi-lidar measurements to correct for projection (Wildmann et al., 2018b; Vasiljević et al., 2017) and automated synchronization to follow the wake meandering (Barthelmie and Pryor, 2019).

Additionally, progress in deployments of scanning lidar and work with observations has begun to be supported by "virtual lidar" models acting on simulations of waked flow. Thus far, virtual lidar studies assessing error behavior in wake scans have
40 typically considered idealized, flat conditions and focused on isolated effects. Doubrawa et al. (2016) investigate how the spatially and temporally disjunct nature of the lidar wake measurements affect the retrieval and highlight the need for adequate spatial distribution of the sampled points. Using three-dimensional, stacked-sector scans performed over 12 min by a lidar colocated with the turbine, observational and virtual measurements are analyzed. The modeled scans are performed in an idealized large-eddy simulation (LES) scenario (inflow based on a laterally periodic LES of the boundary layer) and omit
45 probe volume averaging by the lidar. Meyer Forsting et al. (2017) focus on the effect of averaging over the lidar probe volume, finding the strongest influence on the radial velocities to be in the high-gradient areas around the wake edges. Nacelle-based, continuous-wave and pulsed lidar retrievals of horizontal and vertical planes are modeled in an idealized LES case using a prescribed shear wind profile. The spatial and temporal resolution of the scans are not addressed.

In this study, we assess the influence of scanning lidar retrievals on the properties of the retrieved wake at a complex site
50 following a real case study from the Perdigão field campaign. A mesoscale-microscale nested LES provides realistic inflow conditions for the case study in which we model range–height indicator (RHI) scans made from the ridge downwind of the turbine using a virtual lidar model (Robey and Lundquist, 2022). The simulated measurements in this complex setting are leveraged to perform novel analysis disaggregating and attributing contributions to error in the measured wake due to multiple sources (spatial/temporal resolution of the measurements, averaging over the probe volume, and contamination of the horizontal
55 velocity due to projection of vertical velocities onto the beam), and to address the overall impact on key wake metrics.

Section 2 describes the Perdigão site, selected case studies and data processing, with the setup of the LES and virtual lidar models in Sect. 3. Section 4 describes how the collected wake data are processed into vertical profiles and fitted to quantify the

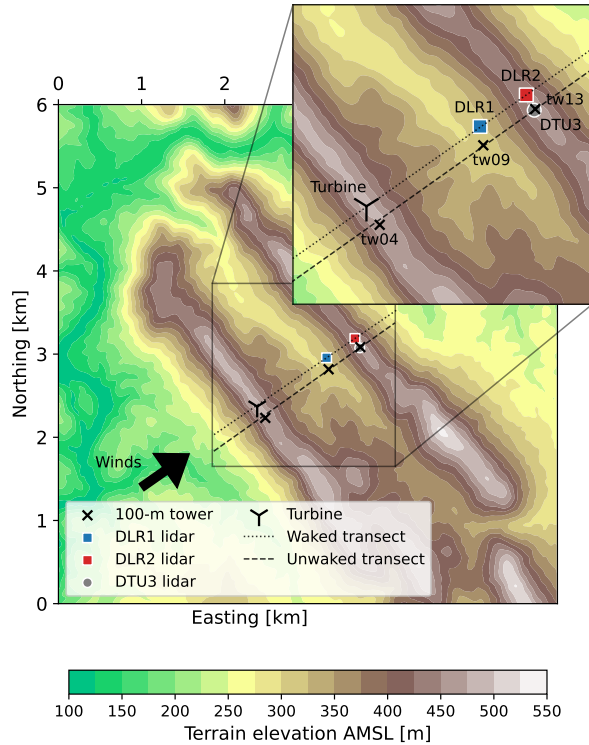


Figure 1. Plan-view topographic map of the Perdigão site over the inner LES domain. Inset of the valley details locations of the turbine, 100 m towers, and the scanning lidars with corresponding transect planes.

wake trajectory, strength, and extent. Section 5 presents results of the virtual LES measurements and distortions and goes on to compare measurements from real observations. A discussion of the results and summary of the key conclusions are given in Sects. 6 and 7.

2 Perdigão campaign and selection of case studies

The Perdigão field campaign, conducted near the Vale do Cobrão in central Portugal, comprised an extensively instrumented investigation of flow over parallel ridges with the intensive observation period spanning from May to June 2017 (Fernando et al., 2019). Dominant climatology at the site features winds perpendicular to the 2 km long ridges. Combined with the symmetry of the ridges and valley, the winds resemble that of idealized, two-dimensional valley flow. Scanning lidars deployed at the site provide insight into the spatial structure of flow dynamics and phenomena. The collected data reflect atmospheric processes appropriate to the regime, including low-level jets, stable mountain waves, and recirculations in the valley (Menke et al., 2019). On the upwind ridge is a single 2 MW Enercon E-82 turbine (78 m hub height, rotor diameter $D = 82$ m), the wake of which was captured as it propagated over the valley in southwesterly flow conditions.

Table 1. Summary of selected case study periods

	Case 1	Case 2	Case 3
Start time [UTC]	21-05 21:30	13-06 4:30	14-06 0:00
End time [UTC]	22-05 01:30	13-06 7:00	14-06 7:30
Duration [h]	4	2.5	7.5
Mean wind speed [m s^{-1}]	6.1	5.7	5.6
Wind speed standard deviation [m s^{-1}]	1.2	0.7	0.9
Mean wind direction [deg]	218	218	218
Wind direction standard deviation [deg]	8	11	9

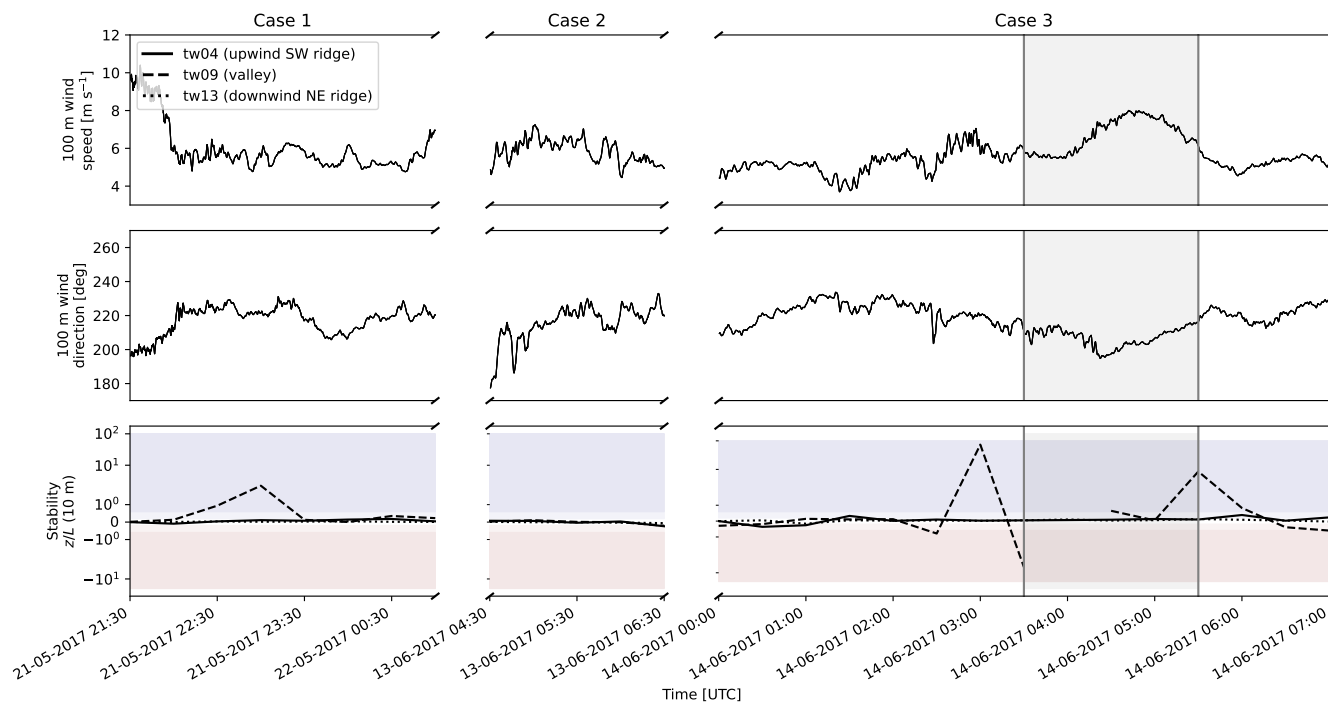


Figure 2. One-minute averaged wind and thirty-minute averaged stability metrics for the three selected case studies. Red and blue shading indicate areas in which the Obukhov stability parameter is unstable and stable, respectively. The gray shaded region within Case 3 indicates the simulation period.

70 We refine a set of stable case studies with winds at operating speeds perpendicular to the ridges so that a significant portion of the wake may be expected in the scanning transect. Using one-minute averaged data from the upwind ridge tower (tw04, Fig. 1), the data are filtered such that the 100 m winds are perpendicular to the ridges (southwesterly, 200°-230°) and at turbine operating speeds ($> 4.5 \text{ m s}^{-1}$, cut in at 2 m s^{-1}). We identified three case study periods with good lidar data that match these conditions for more than two consecutive hours (Table 1, Figure 2). Standard deviations values are given with respect to
 75 the minute averaged wind speed and direction values. The final case overlaps with the high-resolution Weather Research and Forecasting (WRF) LES period from 3:30 to 5:30 UTC on 14 June 2017 (Sect. 3.1).

Stability conditions are diagnosed from the Obukhov stability parameter, z/L , at three towers across the ridges and valley at 10 m and 100 m (Fig. 2). The Obukhov length, L , is defined as

$$L = -\frac{u_*^3 \Theta_0}{\kappa g w' \theta'} \quad (1)$$

80 where u_* is the friction velocity (m s^{-1}), Θ_0 is the average surface potential temperature (K), $\kappa = 0.4$ is von Kármán's constant, $g = 9.81 \text{ m s}^{-2}$ is the acceleration due to gravity, and $\overline{w' \theta'}$ is the heat flux (K m s^{-1}). Turbulent heat and momentum fluxes are computed with a standard eddy-covariance approach from 20-Hz sonic anemometer and 1-Hz air temperature sensor data over a thirty-minute averaging window. The dimensionless z/L parameter indicates stability following the classifications in Rodrigo et al. (2015), symmetrically extending those of Sorbjan and Grachev (2010): nearly neutral ($|z/L| < 0.02$), weakly stable ($0.02 < z/L < 0.6$), and very to extremely stable ($0.6 < z/L$). Over the complex topography of the site, significant variations in the stability parameter can occur, reflected by the variation in the values reported at the different towers. The selected cases are mostly neutral to stable (Fig. 2), conditions under which the wake is expected to be more coherent and detectable (Bodini et al., 2017).

From the available instrumentation, we narrow our focus to three Leosphere WindCube 200S systems performing vertical-slice RHI scans of transects across the ridges (Fig. 1). The positions and scan configurations of the Danish Technical University (DTU) lidar and two German Aerospace Center (DLR) lidars analyzed in this study are detailed in Table 3 (Mann, 2019; Wildmann, 2019). Two lidars operated by DLR scan a transect intersecting the turbine (Wildmann et al., 2018a). With one instrument in the valley and the other on the northwest ridge (Fig. 3), the DLR scans collect data on the waked flow in the perpendicular transect from different vantage points. The final WindCube 200S is part of the DTU long-range wind scanner
 95 system (Vasiljević et al., 2016; Menke et al., 2019) and covers a comparable, unwaked transect separated from the turbine transect by $\sim 125 \text{ m}$.

Alternate scanning approaches are possible, including horizontal planes through the wake and other coordinated scans deployed at Perdigão, that are not treated here. In fixed transect scans such as the ones we use, meandering of the wake can impede measurements as the bulk of the wake may move out of the observed transect. By constraining the cases to those perpendicular
 100 to the ridges, we increase the expectation that a substantial portion of the wake is present in the transect. Acknowledging that the reference truth of the winds in the transect may not represent the full wake in the three-dimensional space, our analysis focuses on the potential observational distortion of the wake as it exists in the transect.

Table 2. Placement and scan parameters of the three lidar systems

	DTU LRWS3	DLR1	DLR2
Instrument height AMSL [m]	452.3	323.2	458.2
Instrument position	39° 42' 48.69" N 7° 43' 49.68" W	39° 42' 44.83" N 7° 44' 6.41" W	39° 42' 52.31" N 7° 43' 52.12" W
Instrument placement	unwaked downwind ridge	waked valley	waked downwind ridge
Azimuth angle θ [deg]	235	237	237
Minimum elevation angle ϕ_0 [deg]	-6	6	-12
Maximum elevation angle ϕ_N [deg]	30	160	90
Elevation angle interval $\Delta\phi$ [deg]	0.75	1	1
Beam accumulation time [s] $\Delta\phi$ [deg]	0.5	0.5	0.5
Scan sweep duration [s]	24	77	51

To control the quality of the lidar data, measurements from all instruments are filtered by the carrier-to-noise-ratio (CNR), requiring $\text{CNR} > -24$ dB. The scans are further averaged over 5 minutes before use (see Sect. 4.1).

105 3 Simulation of flow and lidar instrumentation

3.1 Case study simulation

To better understand the dynamics and action of the lidar systems on the flow, we employ a simulation of the flow field during 2 hours of the 14 June 2017 case study combined with a model of the instrument retrieval. The simulation uses the WRF LES model (Skamarock et al., 2019) and is a reproduction of a validated simulation of the case study with the model (Wise et al., 110 2022). We follow the configurations therein, updated for WRFv4.3 mesoscale-to-microscale (MMC) model and outputting high-frequency (1 Hz) output on which to run the virtual lidar model. As in Wise et al. (2022), five domains are used to nest down from mesoscale, forced by Global Forecast System reanalysis data (National Centers for Environmental Prediction, National Weather Service, NOAA, U.S. Department of Commerce, 2015), down to fine LES scales. This mesoscale-microscale modeling approach allows realistic boundary inflow and forcing in the LES, driven by coarser models of the larger weather 115 systems (Haupt et al., 2019, 2023). The nests refine the horizontal resolution from the outer mesoscale domains with 6750 m and 2250 m horizontal grid size to increasingly fine LES resolution with 150 m, 50 m, and finally 10 m grid spacing in the innermost domain. The outer two domains were allowed to spin up for 9 hours before starting the inner domains. These in turn spin up for an additional 30 minutes before the simulation data are used.

For land input, we use 1 arcsec terrain from the Shuttle Radar Topography Mission (Farr et al., 2007) and 100 m land use 120 data from the CORINE Land Cover 2006 raster dataset (Bossard et al., 2000). We follow adjustments in Wise et al. (2022) to the

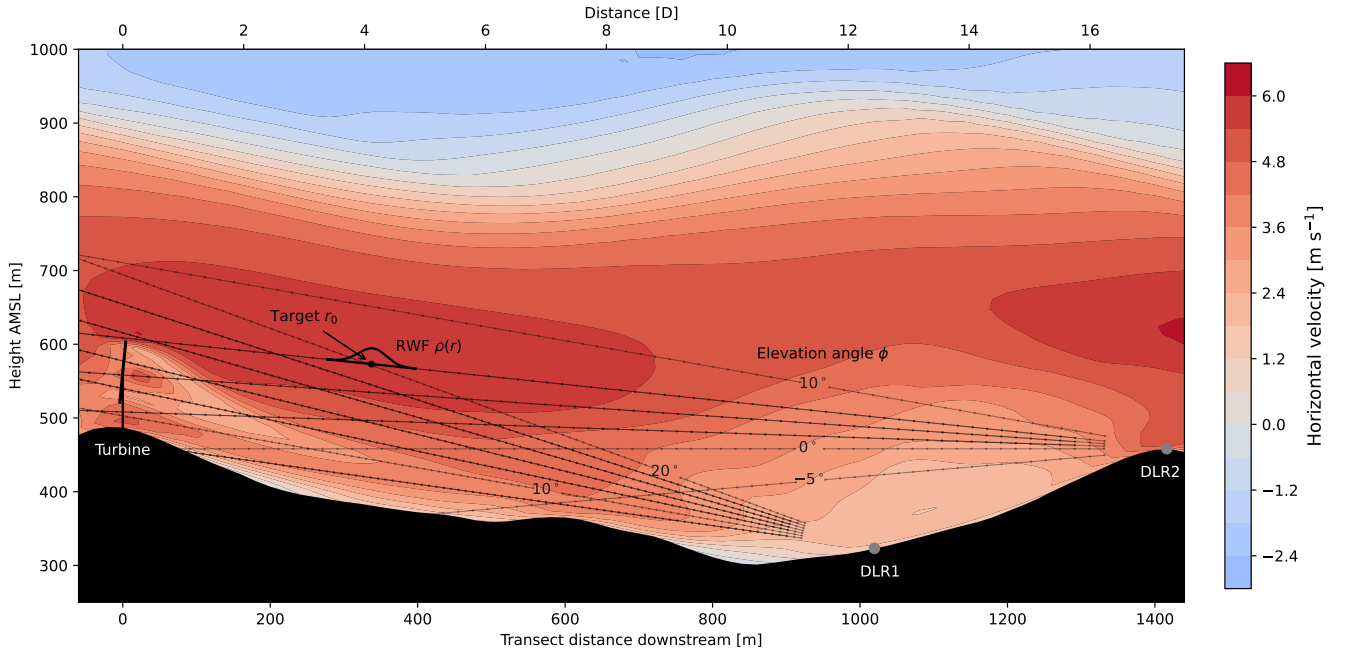


Figure 3. Waked transect cross section with LES horizontal winds and the layout of the turbine and DLR lidars. Sample lidar beams with elevation angles, target retrieval points, and range-gate weighting function (RWF) probe scale are shown for reference. Top axis shows distance in rotor diameters, D .

roughness length of mixed shrubland/grassland to 0.5 m. The turbine feedback on the flow in the finest domain is represented via the generalized actuator disk model in the MMC release (Mirocha et al., 2014). The lift and drag coefficients for the 2 MW E-82 Enercon turbine at the site are not publicly available, so a representative turbine with similar parameters is used in the simulation (Arthur et al., 2020).

125 Inner-domain LES winds are output every second, and the winds on the waked and unwaked transect planes are extracted as a "truth" reference against which to compare the virtual lidar measurements. To represent the raw velocity fields in as unadulterated a way as possible, the velocities are interpolated in the horizontal directions to positions along the transect, with the vertical grid unchanged (Fig. 3). The stretched vertical grid provides sufficient resolution across the wake with 20 points in the lowest 200 m above the surface.

130 3.2 Virtual instrument model and configuration

To represent the lidars in the simulation, virtual instruments are placed in the finest LES domain following deployment locations and scan parameters from the campaign (Table 3). The virtual lidar model mimics the wind retrieval and scanning pattern of the instrument; details can be found in Robey and Lundquist (2022), but we briefly summarize the key points here.

Table 3. WindCube 200S lidar parameters

Fast Fourier Transform Points M [#]	64
Digitization frequency f_s [MHz]	250
Range gate τ_m [ns]	256
Pulse full width at half maximum τ [ns]	200
Probe full width at half maximum Δp [m]	44

Coherent Doppler lidars measure wind speeds at target distances by diagnosing the Doppler shift in laser light that is backscattered by suspended aerosols. Scanning lidars perform an RHI scan by sweeping their beam through a vertical slice of varying elevation angle in time. For the simplified virtual model, we assume uniform and adequate aerosol distribution, omitting aerosol type, size, and density distribution and the influence of conditions like humidity, fog, or precipitation on the return signal (Aitken et al., 2012; Boquet et al., 2016; Rösner et al., 2020).

The virtual lidar model can be considered as a series of stages: interpolation/selection at the location of the retrieval points, projection of the velocities onto the elevated beam, averaging over the probe volume, and advancement of the beam position over the scan duration. References for the beams, retrieval points, elevation angles, and the probe volume weighting are shown in Fig. 3. Note that each of the stages performs a linear operation on the wind field, and error in the estimated horizontal velocity incurred by each is directly additive. The impact of each of the stages on the retrieval may be separated out via partial models using only a subset of the stages.

(1) *Interpolation.* Once the lidar geometry (position and scanning angles) sets the beam location, the wind components are interpolated to points along the lidar beam using linear barycentric interpolation from a Delaunay triangulation of the LES grid (Virtanen et al., 2020; Amidror, 2002). At the retrieval points, this is what the lidar would measure if it could perfectly collect 3D winds.

(2) *Projection.* The wind velocity vector, $\mathbf{u} = (u, v, w)$, is projected onto the beam unit direction vector, $\hat{\mathbf{b}}$. The lidar senses only the radial (line-of-sight) velocity, v_r (Eq. 2).

$$v_r = \hat{\mathbf{b}} \cdot \mathbf{u} = u_h \cos \phi + w \sin \phi \quad (2)$$

where $u_h = u \sin \gamma + v \cos \gamma$ is the horizontal velocity in the transect of the azimuthal angle, γ , and ϕ is the elevation angle of the beam above the horizon. Under this convention, positive radial velocities move away from the instrument.

(3) *Range-gate weighting (RWF).* Due to the lidar measurement process, the radial velocity measured by the lidar at target distance r_0 , $\bar{v}_r(r_0)$, is not a point value but an average of winds in a probe volume along the beam. The averaging is well-represented by a convolution of the projected wind velocities along the beam with a range-gate weighting function, $\rho(s)$ (Eq. 3).

$$\bar{v}_r(r_0) = \int_{-\infty}^{\infty} \rho(s) v_r(r_0 + s) ds \quad (3)$$

Both DTU and DLR systems considered in this study are WindCube 200S lidar systems; we correspondingly use a model for a pulsed RWF (Eq. 4), based on the convolution of the pulse with the range-gate observation window (Banakh and Smalikho, 1997; Cariou and Boquet, 2010).

$$\rho(r) = \frac{\operatorname{erf}\left(\frac{4\sqrt{\ln 2}}{c\tau}r + \frac{\tau_m\sqrt{\ln 2}}{\tau}\right) - \operatorname{erf}\left(\frac{4\sqrt{\ln 2}}{c\tau}r - \frac{\tau_m\sqrt{\ln 2}}{\tau}\right)}{c\tau_m} \quad (4)$$

Here, c ($0.29979 \text{ m ns}^{-1}$) is the speed of light and $\tau = 200 \text{ ns}$ is the full-width half-maximum (FWHM) of the Gaussian pulse used by lidar system. The range-gate observation time, τ_m , arises from the window for the fast Fourier transform (FFT) used for the frequency diagnosis. With M points of a signal digitized at a frequency of f_s , the range-gate window is $\tau_m = Mf_s^{-1}$. We use consistent sampling settings across all three WindCube 200S based on the values reported in the DTU lidar data files and summarized in Table 3 (Mann, 2019). The temporal window corresponds to a spatial probe length, Δp , over which the contributions to the signal originated. An estimate of Δp is given in Banakh and Smalikho (1997) as the estimate of the FWHM of the RWF (Eq. 5).

$$\Delta p \approx \frac{c\tau_m}{2\operatorname{erf}\left(\sqrt{\ln(2)}\frac{\tau_m}{\tau}\right)} \quad (5)$$

For this system, $\Delta p \approx 44 \text{ m}$, which aligns with visual inspection of the modeled RWF curve (shown for reference in Fig. 3). Probe lengths of 30 m have been reported by Menke et al. (2019), which may arise from altered parameters or different approaches to the RWF model and estimation.

In the virtual lidar model, the weighting integral of the radial velocities by the RWF (Eq. 3) is approximated by a discrete weighted average using interpolated velocities at positions s_k along the beam, spaced every 1 m (Eq. 6).

$$\bar{v}_r(r_0) \approx \sum_k \frac{h_k \rho(s_k - r_0)}{\sum_i h_i \rho(s_i - r_0)} v_r(s_k) \quad (6)$$

When the probe volume intersects with a hard object, the strike can corrupt the wind data; the model accounts for blocking of the beam due to terrain by requiring valid points reaching 80% of the RWF volume. Contamination due to hard strikes of the turbine, which do occur in the actual data, are not replicated.

(4) *Time-staggering.* The sweep of the beam over the duration of the scan is realized in time by staggering the retrieval of the radial velocities over the high-frequency (1 Hz) LES output. Some of the real instruments adjusted the beam every 0.5 s , and linear interpolations between the LES output are used for these intermediate times. We further note that this model does not currently include continuous scanning collecting data from over the arc of travel; the beam retrievals reflect fixed, incremented positions.

185 4 Wake fitting

4.1 Construction of deficit vertical profiles

Our analysis concerns distortions of the wake in the two-dimensional transect plane. In order to quantify and characterize the wake and allow for comparison of true and observed behavior, we construct vertical profiles of the horizontal velocity

deficit downwind of the turbine. Construction of the vertical deficit profiles entails estimation of the horizontal velocities from
 190 line-of-sight velocities, interpolation of the irregular data to the vertical profiles, and time averaging to allow for a robust
 comparison between waked and unwaked transects to isolate a wake deficit. Processing of the wake is identical for virtual and
 (quality-controlled) observational data.

To estimate the horizontal velocity from radial velocities, v_r , the projection of the vertical velocity is assumed to be negli-
 gible, meaning that the radial velocities are purely a projection of the horizontal velocity. Equation 7 solves for the horizontal
 195 velocity under this assumption.

$$u_{h,\text{lidar}} = \frac{v_r}{\cos \phi} = u_h + w \tan \phi \quad (7)$$

where ϕ is the beam elevation angle. The assumption is robust so long as $u_h \gg w \tan \phi$. Significant vertical velocities do occur,
 given the complex terrain and wake, and can lead to error in the estimate due to the inclusion of non-negligible projection of
 the vertical velocity. When relying on a single lidar, limiting the elevation angles of the beams can help to constrain the degree
 200 of contamination from vertical velocities. Here, the beams scanning the upwind ridge in the area of the wake typically have
 elevation angles of $\phi < 20^\circ$ ($\tan 20^\circ \approx 0.36$).

We prescribe vertical profiles along the transect every 20 m ($\sim D/4$) downstream of the turbine with 2 m resolution verti-
 cally. The lidar-recovered horizontal velocities are linearly interpolated to the profiles from the irregular retrieval points using
 a Delaunay triangulation as in Iungo and Porté-Agel (2013). Vertical profiles for the unwaked transect are also computed.

205 To determine the wind deficit, we leverage the symmetry of the campaign site and define the unwaked transect to be the
 freestream velocity, $u_{h,\text{unwaked}}$. To obtain a more robust profile and temper localized variations in the flow between transects,
 the data are time-averaged. We found, with both LES and observational data, that a 5-minute average is sufficient to find good
 agreement between the vertical profiles in the waked and unwaked transects and produce well-defined wake deficits. The period
 corresponds to about 3 RHI sweeps for DLR1, 6 for DLR2, and 13 for the reference DTU3 (and 300 snapshots in the 1 Hz
 210 LES wind field). Only full RHI lidar sweeps are used; for a given 5-minute window, if any beams have a timestamp within the
 window, the whole sweep is included in the average. Longer averaging windows (e.g., 10 or 30 minutes) are possible, but a
 shorter window preserves more of the fast dynamics of the wake.

Aligning the transects, we compute the velocity deficit (Eq. 8) from the corresponding time-averaged vertical profiles of u_h :

$$\Delta u_h = \left(1 - \frac{u_{h,\text{waked}}}{u_{h,\text{unwaked}}} \right) \times 100 \% \quad (8)$$

215 where Δu_h is the percent reduction in wind speed.

The true LES wake deficit is also defined by the difference in flow between the waked and unwaked transects so that wake
 errors arise purely from the influence of the observation system. Here, the raw representation of LES flow field is designed
 to be as minimally processed as possible; the winds are only horizontally interpolated to the locations of the vertical profiles
 along the transect and left on the native vertical grid. Time averages occur across constituent 1 Hz output and determination of
 220 the deficit is performed via a difference between waked and unwaked transects as with the lidar data. The profile construction
 process standardizes the LES, virtual measurements, and observations into the same format with the deficit profiles reflecting
 the wake.

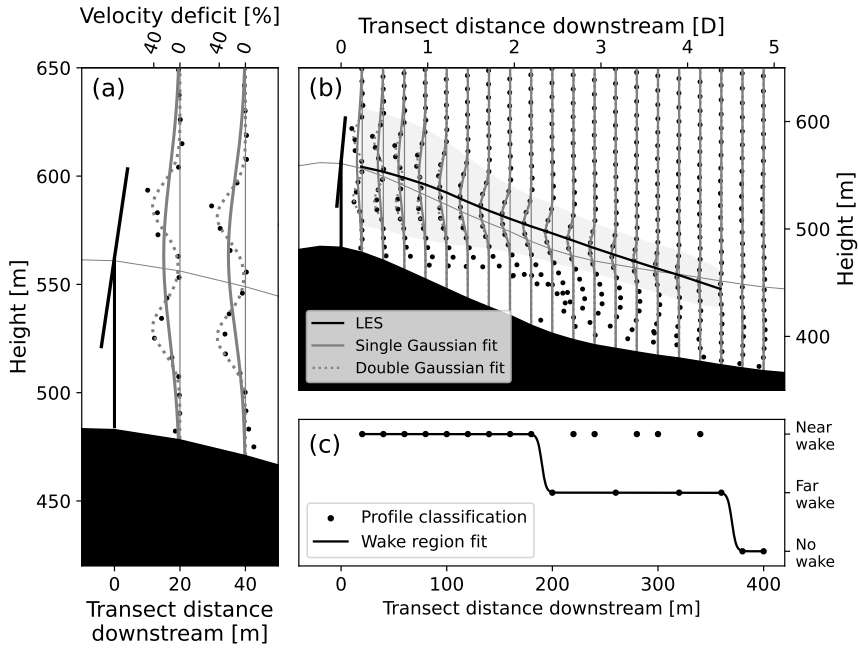


Figure 4. Example wake fit. Single- and double-Gaussian wake models fitted to (a) first few vertical wind deficit profiles and (b) over the larger wake, moving left to right, and highlighting the wake center and extent. (c) Classifications of the individual vertical profiles are fitted into cohesive wake regions.

4.2 Wake-fitting algorithm

To distill and quantify the behavior of the wake and facilitate inter-comparison, both against the LES truth and between
 225 measured wakes, we fit Gaussian models (Eqs. 9,10) to the vertical profiles and extract the magnitude, center height, and
 vertical extent of the wake following the approach in Aitken et al. (2014).

As the winds flow past the turbine and interact with the aerofoil blades, we can sketch the wake. Maximum drag on the
 wind field typically occurs midway along the blade, leading to two distinct local maxima in the wind deficits close to the rotor
 (the near wake) (Martínez-Tossas et al., 2015). As these lobes propagate downstream, they expand and mix with the ambient
 230 turbulent flow and eventually merge and become indistinguishable (the far wake). The deficit diminishes and the wake finally
 dissipates. To capture the range of behavior over the wake extent, a combination of Gaussian models are used.

In the far wake where the lobes have merged, the vertical deficit profile is modeled as a single Gaussian (Eq. 9).

$$g_1(z) = a \exp \left[-\frac{1}{2} \frac{(z - z_c)^2}{\sigma^2} \right], \quad (9)$$

Here, a is the maximum magnitude of the deficit and z_c is the vertical location of the center of the wake. The width of the
 235 Gaussian is controlled by the parameter σ ; we take the corresponding vertical extent (width) of the wake to be the full width at
 which g_1 has decayed to 5 % of the maximum, i.e., $2\sqrt{2\ln(20)}\sigma$.

In the near-wake, where two separate wake lobes are present, the deficit profiles are better represented by the superposition of two symmetric Gaussians (Eq. 10).

$$g_2(z) = a \left(\exp \left[-\frac{1}{2} \frac{(z - z_c + \frac{1}{2} z_{sep})^2}{\sigma^2} \right] + \exp \left[-\frac{1}{2} \frac{(z - z_c - \frac{1}{2} z_{sep})^2}{\sigma^2} \right] \right) \quad (10)$$

240 where the center of the wake, z_c , is the mean between the centers of the two lobes, separated by a distance z_{sep} . The parameters a and σ control the amplitude and width (vertical extent) of the component Gaussian curves. We define the wake maximum deficit to be $\max_z |g_2(z)|$ (not necessarily equal to the parameter a as the separation between the two lobes shrinks). Consistent with the single Gaussian fit, the vertical extent is defined as the full width at which g_2 has decayed to 5% of maximum (note that this definition is not trivially expressed as a constant multiple of the parameter σ and is estimated iteratively from the fitted
245 function g_2).

We deviate slightly from previous approaches in our formulation of the wake fit. The double Gaussian (Eq. 10) is expressed in terms of the full wake center, z_c , and separation between the lobe centers, z_{sep} , in order to more easily place bounds on these parameters. The definitions of the wake magnitude and extent for the double Gaussian fit g_2 also differ from previous estimates; we try to keep the definitions intuitively consistent with the behavior of the wake and the single Gaussian at the
250 expense of having simple expressions in terms of the fit parameters a and σ (see Appendix A for details).

A nonlinear least-squares fit is performed for both of the Gaussian models (Eqs. 9 and 10) on each of the vertical velocity deficit profiles, moving sequentially downstream of the turbine. To isolate potential wake behavior we use the profile data below 700 m where the deficit falls between -10 % and 100 %. The first profile fit is seeded with hub-height center, z_c and an amplitude of $a = 40$ %. The single Gaussian uses a seed $\sigma = 0.5D$ while the double Gaussian uses $\sigma = 0.3D$ and lobe
255 separation $z_{sep} = 0.5D$. The fitted parameter values are then used to seed the subsequent profile fit downstream. We constrain the parameter space toward finding physical wake behavior as follows. We restrict a to lie between 0 and 90 % (Porté-Agel et al., 2020) and the center height z_c between 20 and 200 m above the ground. The first profile fit is pinned more closely to the hub height by taking z_c to be within 10 m at 20 m downstream for the LES and within 50 m at the first profile 100 m downstream in observations. For the single Gaussian we confine σ between 0 and $D[0, 1.5D]$ and for the double Gaussian we
260 use $\sigma \in [0, 0.5D]$ and $z_{sep} \in [0, 0.75D]$. To encourage the fit to follow a cohesive wake structure, we restrict the parameters so that the wake center is within 10 m of the previous fit and the height of the wake is within 80 - 120 % of the previous fit. We emphasize that utility in the wake fitting is in providing an accurate quantification of the wake characteristics and choices in parameter ranges are imposed to nudge the Gaussian fit toward the evident wake structures that occur in the datasets.

Each profile is classified as near wake, far wake, or as having no credible wake detected. Rather than determining the
265 presence of distinct double lobes by a statistical F test, requiring the double Gaussian fit to be significantly better (Aitken and Lundquist, 2014), we take a different approach based on the idea of the physical convergence of the lobes. When the two Gaussian lobes become so close relative to their width that they have merged, set heuristically here by $z_{sep}/w < 2.2$, it is considered to be part of the far wake (see Appendix A). The wake is considered to have dissipated once the deficit magnitude decays to 5 % of maximum. Any profile further downstream from where a fit has reached $a \leq 5\%$, or a has otherwise reached
270 a minimum, is classified as having no wake with fits considered spurious.

Thus, each profile is given a preliminary, individual classification as (2) near wake with two lobes, (1) far wake with a single lobe, or (0) no wake based on its Gaussian fit. In order to determine coherent wake regions, treating the set of profiles as a whole, the preliminary profile classifications are fitted to a two-tiered logistic function (Eq. 11) using the nonlinear least-squares method. We use a variation on logistic regression, which is used in binary classification methods (e.g. Spitznagel
 275 (2007)), to help create a map between the downstream distance and wake region classifications that adhere to the physical transition from near to far to no wake (Fig. 4(c)).

$$\ell(x) = 2 - \frac{1}{1 + \exp[-k(x - x_0)]} - \frac{1}{1 + \exp[-k(x - x_1)]} \quad (11)$$

To ensure a sharp transition between two profiles, we take $k = 10$ to be fixed. The parameters x_0 and x_1 are determined from the functional fit and give the distances at which the wake transitions from near to far and far to dissipated, respectively. Note
 280 that the fitting process helps to filter out non-physical variations in the preliminary classification of the individual profiles (e.g., Fig. 4(c) around 220 and 320 m downstream).

The completed wake fit and corresponding wake characteristics (center position, vertical extent, and deficit magnitude) uses the fitted Gaussian model for the determined wake region, i.e., the double Gaussian fit for profiles in the classified near wake and the single Gaussian fit for profiles in the classified far wake.

285 5 Results

5.1 LES evaluation of wake observation

In the raw LES flow field, a resonant mountain wave forms over the ridges, much as was observed in the field, and the generalized actuator disk turbine model produces a wake with relatively detailed structure (Fig. 3). The maxima in the drag profile of the blade aerofoils lead to the characteristic dual-lobe structure in the near wake, which merges into the far wake
 290 before dissipating. The wake trajectory roughly follows the terrain with the tail of the wake occasionally detaching and lofting a little higher.

In the unwaked transect, the single DTU lidar captures the background flow well, placing the mountain wave and recirculation zones accurately and reproducing all but the most extreme velocity magnitudes (not shown). Errors in the horizontal velocity profiles around the reference region for the wake are consistently small ($< 0.1 \text{ m s}^{-1}$). The accuracy of these mea-
 295 surements is contingent on the smaller spatial and temporal scales in the undisturbed flow compared to those of the lidar probe volume and sweep time, as well as the low beam elevation angles. Because the background flow is captured with high accuracy, it is expected that distortions in the detected wake arise primarily from the measurement of the waked flow itself.

As opposed to flow structures in the freestream transect, smaller spatial scales similar to lidar probe length of 44 m and more rapid variations on the order of minutes pervade the wake and are more prone to producing error in all of the components
 300 of the observation system. Separating the linearly additive stages of the virtual lidar model (Sect. 3.2), we can assess the influence of the resolution of the retrieval points over the wake, the beam projection angle, the RWF probe weighting, and the sweep duration on the measured horizontal velocity profile. Figure 5 shows the linear contribution to the total error in the

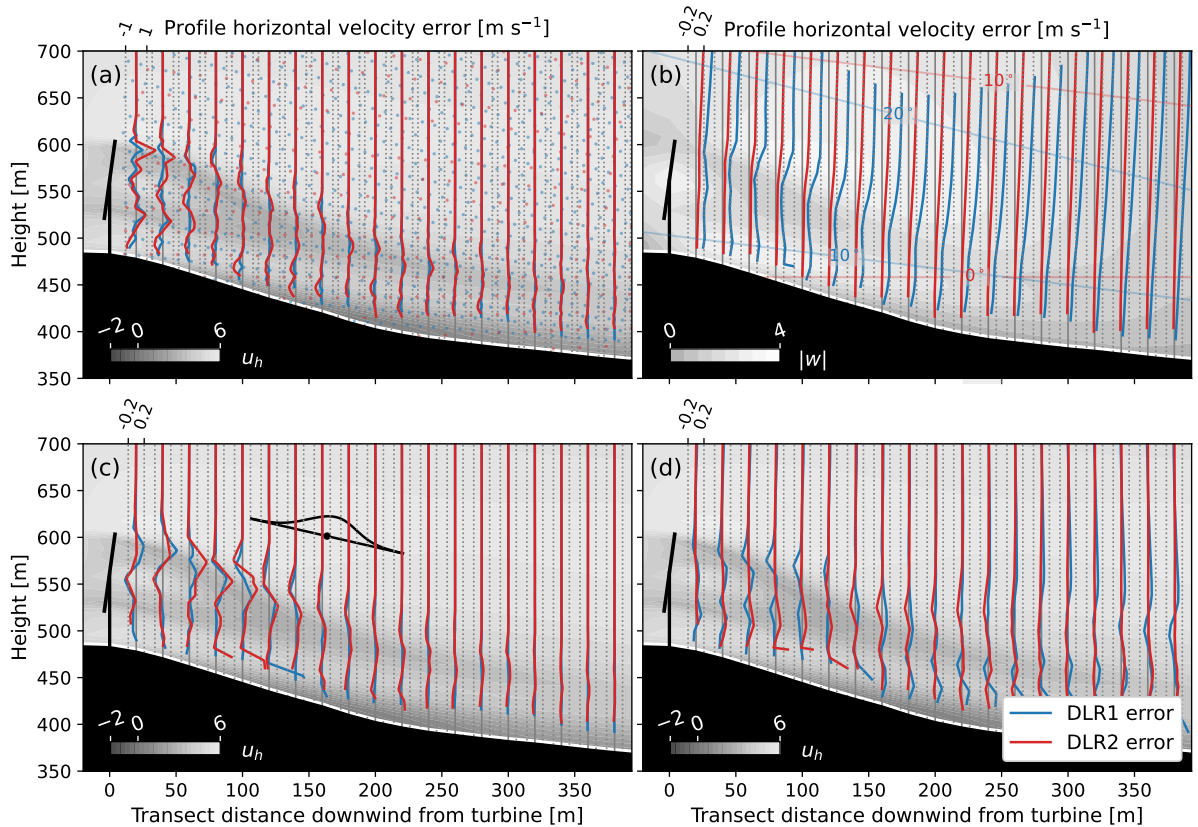


Figure 5. Representative snapshot of contributions to error in lidar-derived horizontal velocity profiles due to (a) the position of the lidar retrieval points, (b) contamination by projection of vertical velocity onto the beams, (c) averaging over probe volume through the RWF, and (d) the duration of the scan sweep. Background contours of the LES horizontal (a,c,d) and vertical (b) winds show the wake for reference. Lidar retrieval points, beam elevations, and the RWF are shown for reference in (a), (b), and (c), respectively.

horizontal velocity profiles downwind of the turbine due to each of these sources.. Errors are computed with respect to the “true”, underlying LES flow field. Each of the stages reacts to the wake in a way not seen with the background flow.

305 The largest contribution to the error in the horizontal velocity profile is due to the spatial resolution of the lidar measurement points,, with values as large as 1 m s^{-1} , and occur most strongly at the edges of the near wake (Fig. 5(a)). Averaging effects of the RWF over the probe volume reach up to 0.5 m s^{-1} and are most pronounced around the upper wake boundary (Fig. 5(c)). Error incurred due the duration of the scan sweep can occasionally be as large as 0.5 m s^{-1} , peaking around the edges and tail of the wake and during more transient conditions early in the case study (Fig. 5(d)). The error contribution from the

310 projection of the vertical velocity is generally less than 0.2 m s^{-1} near the wake (Fig. 5(b)), where the magnitude of the error grows higher up in the profiles where the elevation angles of the beams are greater.

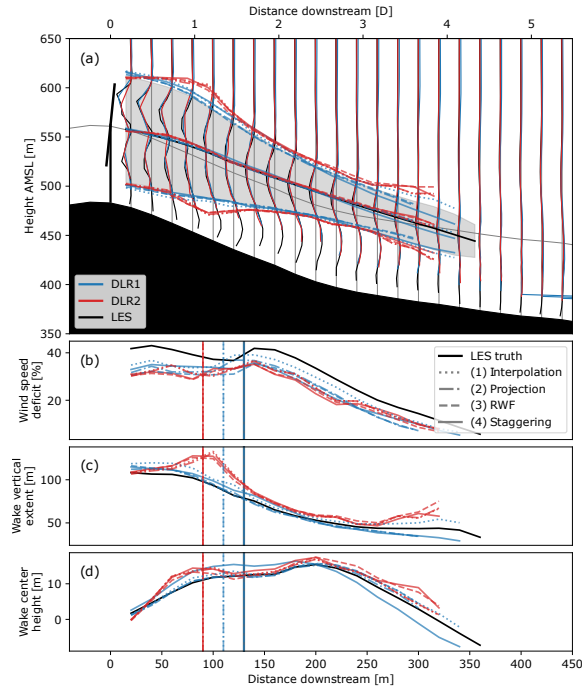


Figure 6. (a) Vertical deficit profiles for true LES wake and those measured using the DLR lidars along with the detected wake center line and width. Comparison of detected (b) maximum magnitude of the wake, (c) vertical extent of the wake, and (d) height of wake center relative to terrain-following hub height. Vertical lines show where the fit transitions from a double to single Gaussian, i.e., near to far wake.

Differences in the positioning and geometry of the two DLR lidar scans provide insight into the variation between altered configurations (reflected in the red and blue lines in Fig. 5). Larger interpolation errors using the DLR2 system evidence the wider spacing between range gates (20 m versus 10 m) and further downstream distance (1000 m versus 1400 m), enlarging the distance between beams at the same angular resolution (1°). We estimate DLR2 to have a density of about 0.002 retrieval points per square meter in the area of the wake compared to 0.006 points per square meter for DLR1. The positioning of the lidar also consequently changes the angle of the beams intersecting the wake and therefore the projection and the behavior of the RWF, with the probe volume cutting through and incorporating distinct parts of the wind field. Errors due to the scan duration are marginally larger for DLR1, which takes 77 s to arc across the entire valley to the other ridge, compared to DLR2, which only sweeps to vertical over 51 s. Overall, though differences in the configurations impact components of the error in understandable ways, the geometries are not radically dissimilar, and much of the behavior is echoed across the two systems.

Even moderate systematic errors in the velocity field can distort the perceived wake behavior, quantified via the fitted deficit magnitude, vertical extent, and height of the wake center. For a single 5-minute window, we compare the fitted wakes from the time-averaged LES profiles with those from the virtual lidar data (Fig. 6). The wake fits after incorporating each observation stage to the lidar model are compared to elucidate their effect on the retrieved wake. While informative, we caution that the

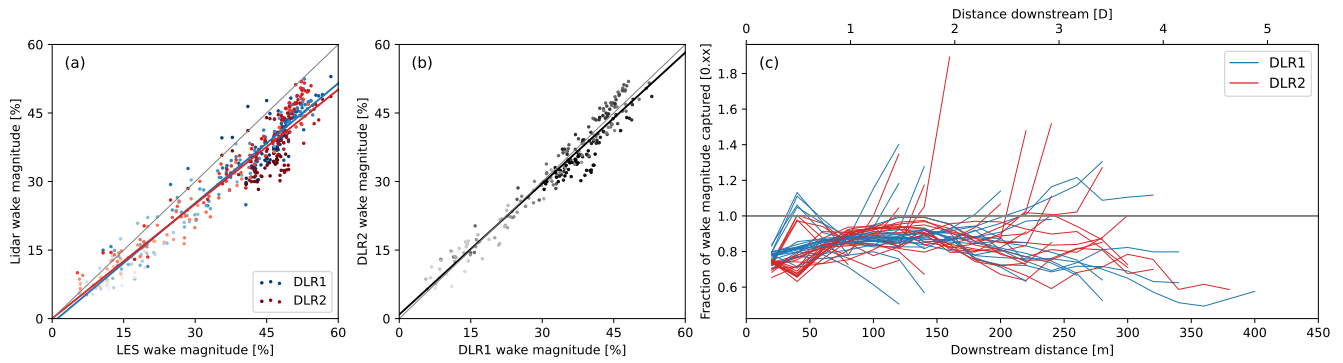


Figure 7. Magnitude of the wake deficit with darkest to lightest hues indicating increasing distance from turbine comparing (a) DLR-recovered value plotted against LES truth and (b) DLR instruments plotted against one another with the least-squares best-fit lines. (c) Fraction of maximum LES wake deficit magnitude captured by the two DLR lidars over wake extent for each 5-minute window.

fit operation is nonlinear, so the contribution from the observation stages can no longer be considered additive. In the overall structure of the wake, we observe that the distinction of the two lobes in the near wake is lost too early in the lidar retrievals (Fig. 6). The early transition exists in the lidar model using only interpolation and may be explained primarily by insufficient resolution of the retrieval points. For DLR1, which has finer resolution than DLR2, RWF averaging also contributes. The DLR1
 330 beams cut through the wake at a steeper angle that may cause more significant smoothing along the vertical axis, blurring the distinction of the lobes.

The wake deficit magnitude, vertical extent, and center position are shown in Figs. 7-10, plotting the lidar retrieved values against the LES truth as well as directly against one another and showing the error in the retrievals over the the wake extent. The root-mean-square deviation (RMSD) between the the compared retrievals and metrics for the best-fit least-square lines
 335 summarized in the first columns of Table 4.

Using the full lidar model, we show the comparisons of the wake characteristics in aggregate. The wake deficit magnitude, vertical extent, and center position are shown in Figs. 7-9 plotting the lidar retrieved values against the LES truth as well as directly against one another and showing the error in the retrievals over the the wake extent. The root-mean-square deviation (RMSD) between the true and measured wakes and metrics for the best-fit least-square lines summarized in the first columns
 340 of Table 4.

The maximum velocity deficit magnitude is consistently underestimated by both lidars. Figure 7 compares the recovered deficit against LES in aggregate and tracked over the length of the wake. In the bulk of the wake, only around 0.85 of the maximum wake deficit is reflected in the lidar retrieval (Fig. 7, Table 4). The disaggregation of the stages (Fig. 6(b)) suggests that much of the loss of the peak has already occurred due to the limited resolution of points across the wake and is exacerbated
 345 by the further RWF averaging effects over the probe volume. Conversely, elongation and overestimation of the deficit can occur at the tail of the wake, driven by the probe volume (RWF); measurements made at target points beyond the wake can incorporate slower waked winds from upstream, causing unwaked points to appear to be waked and blurring the wake bounds.

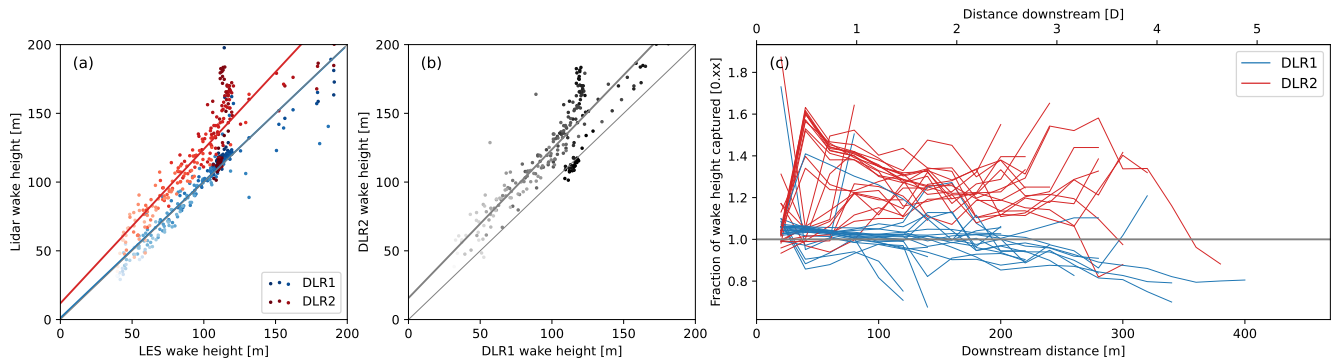


Figure 8. Vertical extent of the wake with darkest to lightest hues indicating increasing distance from turbine comparing (a) DLR-recovered value plotted against LES truth and (b) DLR instruments plotted against one another with the least-squares best-fit lines. (c) Fraction of LES wake height captured by the two DLR lidars over wake extent for each 5-minute window.

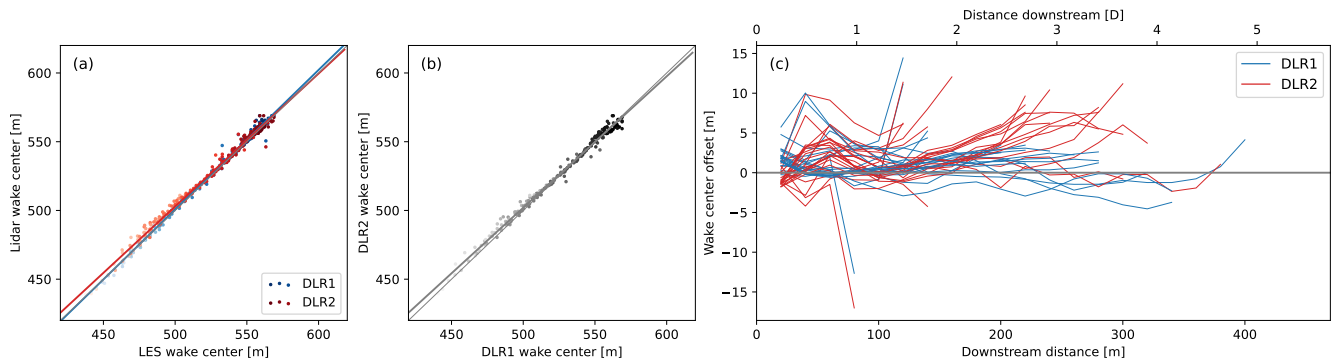


Figure 9. Height of the wake center with darkest to lightest hues indicating increasing distance from turbine comparing (a) DLR-recovered value plotted against LES truth and (b) DLR instruments plotted against one another with the least-squares best-fit lines. (c) Difference in the LES wake center height and that captured by the two DLR lidars over wake extent for each 5-minute window.

The DLR2 system on the far downwind ridge consistently experiences greater deficit loss in the near and middle wake, likely driven by the coarser spatial resolution of the retrieval points identified in the horizontal velocity error. Because both systems underestimate the magnitude, the difference between the two is minor compared to the initial loss in the maximum deficit.

The vertical extent of the wake in the retrieval is particularly subject to the error noise in the horizontal velocity that occurs around the wake bounds. The wake measured by DLR2 has a height inflated by about 12 m relative to the reference LES, whereas DLR1 is more accurate with errors typically less than 13 m (Fig. 8, Table 4). Interpolation from retrieval points explains most of the difference for DLR2. With DLR1, the distortion is mostly in the tail of the wake and seems to arise once projection effects have been incorporated (Fig. 6(c)).

		Simulated Case 3			Observation DLR1 vs DLR2		
		LES vs DLR1	LES vs DLR2	DLR1 vs DLR2	Case 1	Case 2	Case 3
Magnitude	Fit intercept [%]	-0.95	0.03	0.88	-1.54	9.46	7.74
	Fit slope [-]	0.87	0.83	0.96	0.79	0.80	0.86
	Correlation coefficient r [-]	0.97	0.95	0.97	0.83	0.94	0.95
	RMSD [%]	6.84	7.69	2.76	16.53	6.64	8.63
Height	Fit intercept [m]	1.16	11.83	15.65	74.52	77.10	53.61
	Fit slope [-]	0.99	1.12	1.08	0.76	0.55	0.67
	Correlation coefficient r [-]	0.92	0.89	0.90	0.52	0.71	0.79
	RMSD [m]	12.41	29.86	29.26	84.10	51.70	31.95
Center	Fit intercept [m]	-7.34	19.69	24.36	-38.65	55.58	34.23
	Fit slope [-]	1.02	0.97	0.96	1.05	0.89	0.94
	Correlation coefficient r [-]	1.00	1.00	1.00	0.72	0.85	0.96
	RMSD [m]	2.54	3.81	3.14	18.60	12.06	6.25

Table 4. Root-mean-square deviation (RMSD) and linear least-squares fit metrics for comparisons of wake magnitude, height, and center using virtual and observational retrievals.

The trajectory of the wake, tracked via the center of the deficit Gaussian, is the most accurate of the metrics and has the least variability between the two systems (Fig. 9, Table 4). The retrieved position is often offset less than 5 m from the LES reference and rarely exceeds 10 m. Differences between the two systems are minor. DLR2 does suggest a slightly higher trajectory than DLR1 in the tail of the wake and appears to be more sensitive to how the RWF probe volume cut through the wake. The positioning of the wake tail by DLR1 is more significantly affected by the longer scan time, likely due to the more transient behavior of this part of the wake (Fig. 6(d)).

5.2 Comparison of observations in field data retrievals

Using data from the three field campaign case studies, spanning 840 total minutes (168 5-minute windows), the same wake data processing successfully yields well-defined wake deficits. For observations, a truth reference is not available, but the independent retrievals from the two DLR lidars may be compared against one another to estimate potential variation due to system configuration (Fig. 10). A similar inter-comparison can be done using the virtual instruments (as shown in panel (b) of Fig. 7- 9) so that the approach can simultaneously validate the model as a representation of the behavior of the real data.

We note that the unwaked reference measured by the DTU lidar is used throughout, so the comparison isolates differences in how the two DLR lidar scans collect the wake. In the LES analysis, important distortions, such as the systematic underestimation of the wake deficit magnitude, existed similarly across both systems and are not evident in the inter-comparison between systems.

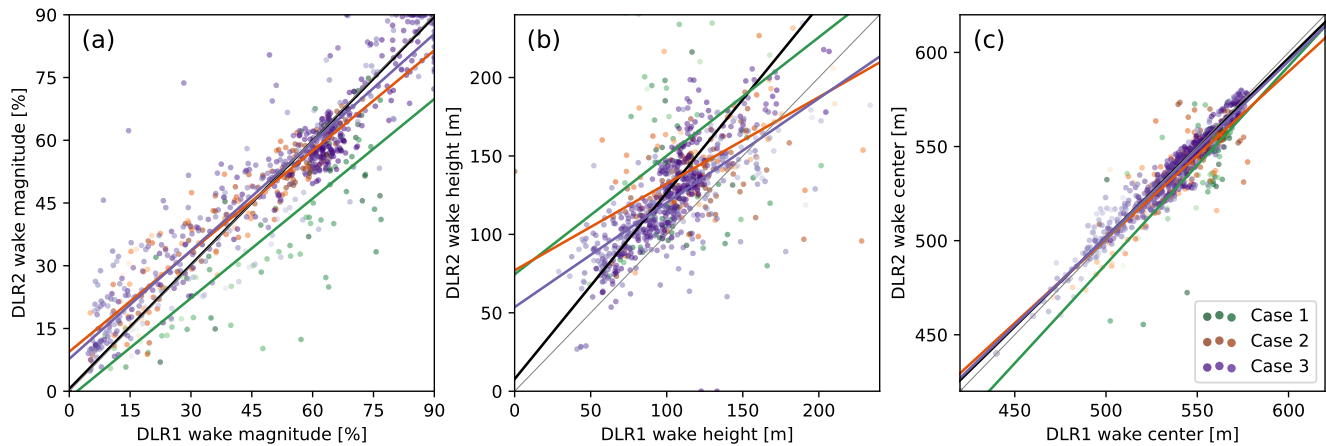


Figure 10. Comparison of wake (a) maximum deficit magnitude, (b) vertical extent, and (c) center height position retrieved by DLR1 and DLR2 in the observational case studies. Darkest to lightest hues indicating increasing distance from turbine. The black lines show the best-fit from the virtual instruments in the LES subcase.

Over the course of the selected cases, the observational data reflect a wider range of wind speeds, more transitory conditions, and greater variety of wake behavior than is covered by the limited simulation period. Evident wake structure in the deficit profiles occurs in about 86 % of the 5-minute windows. The wake in Case 1 typically follows the terrain line at just above hub height, but occasionally lofts higher. Velocity deficits are high and the wake often persists far downstream (up to $7 D$). There are frequent instances of the wake extent growing with distance, a case neglected in the LES, where the wake almost universally tapered to dissipation. Case 2 is qualitatively similar to Case 1 though it experiences shorter wakes and weaker initial velocity deficits. Case 1 features the fastest wind speeds and the wake appears to be completely detached from the terrain variation and lofts out directly from the hub height.

The comparisons of the observational wake characteristics are noisier due to the nature of the raw data and imperfections in the wake fitting algorithm. The observational deficit profiles are subject to additional noise from the lidar systems due to factors like pointing accuracy of the lidar beams, small-scale turbulent behaviors unresolved by the LES, complex aerosol distributions affecting returns, among other complexities. While the fitting algorithm produces good fits about 90% of the time, it does have shortcomings in robustly handling the full range of behavior in the observations. Frequent issues are a lack of clear truncation point in low-deficit regions and apparent deficit behavior near the surface due to differences in the transect terrain, which causes the fitted center to track low or the wake signal to be obfuscated.

The wakes retrieved by the two DLR systems show marked differences. Trends comparing wake magnitude, height, and position largely align with those of the modeled lidar in the LES (Fig. 10, Table 4). Predictably the best agreements are with Case 3, which most closely matches the conditions in the LES and has the best quality and quantity of observational data. The consistency provides confidence in the ability of the model to predict wake measurement behavior in these conditions.

In the deficit magnitude, Cases 2 and 3 reflect predictions from the virtual instruments in which DLR1 reads slightly higher maximum deficits in the near wake and slightly lower in the far wake (Fig. 10(a)). In Case 1, DLR1 consistently retrieves wakes with a more significantly lower deficit throughout. As in the simulations, the correlations between instruments is strong, though there the overall variability between the two is higher (6–17 % compared to about 3 % RMSE).

395 The vertical extent of the wake experiences the most variability between DLR1 and DLR2, even more so than seen in the LES 10(b)). Because of the large variations, the linear fits are less representative. In Case 3, deviations between the two retrieved wakes often reach 30 m, a value consistent with the virtual lidar comparison. The other cases see even more dramatic discrepancies and are marginally correlated.

The trajectory of the wake center in the retrievals agrees well as anticipated. The correlation is high and the linear fits have slopes close to unity. In Case 3, differences are typically within about 6 m, compared to 3 m with the virtual instruments. Case 400 2 is similar with a larger spread. Differences are more substantial in Case 1, and we note that for some windows, the differences in positioning and behavior is evident in the raw deficit profiles.

6 Discussion

All of the components of the lidar observation system – the resolution of retrievals in space and time, projection onto the beam, 405 and RWF averaging over the probe volume – are prone to more significant error when measuring the heterogeneous wake than the more homogeneous background flow as the spatial and temporal scales of the wake compete with those of the lidar system and additional vertical velocities are induced in the wake. We caution that the particular distortion behavior is specific to the wake dynamics of any particular time and the geometry of the scan, but insights and generalizable trends can be drawn from the results. Further, the virtual lidar methodology presented here could be applied to other scan types and geometries.

410 Insufficient spatial resolution of the retrieval points and the smoothing effect of the RWF, which incorporates faster winds in the probe volume, can cause the lidar to miss the largest velocity deficits, underestimating the strength of the wake. Particularly close to the turbine, these underestimates can be significant. In the far wake, the trend can flip and the lidar sometimes overestimates the magnitude of the wake deficit. Especially near the tail of the wake, the RWF capturing much slower points upwind prevents the measured wake from decaying as quickly as it does in reality. Correspondingly, this effect can cause the 415 measured wake to be longer than in reality when the probe volume still contains waked winds.

In context with other error sources, we highlight the potentially dominant contribution to error in horizontal velocity measurements due to under-sampling the wake region. Though in a more complex setting and a different, and faster, scan approach, we find as in Doubrava et al. (2016) that diagnosis of the wake center is typically less sensitive to the coarser sampling than other features of the wake. The retrievals by DLR1 compared to DLR2 illustrates how an increased sampling density can improve the fidelity of the measured wake. The advantage is clear despite larger beam elevation angles and a longer scan sweep. 420 We emphasize that the DLR scans both included large angular sectors and corresponding long scan durations (51, 77 s); the balance of errors suggests that long scans performing spatially dense sweeps may be a reasonable trade-off.

For our downwind measurement scenario, the error contribution from the RWF averaging effects echo those in Meyer Forsting et al. (2017) with nacelle-based scans in that the largest RWF averaging effects occur near the large gradients at the edges of the wake. The RWF can smooth the edges of the wake, inflating the measured bounds and making it seem taller and longer. While different configurations and technologies (pulsed vs continuous wave) exist that impact the shape and scale of the RWF, practical considerations in obtaining robust velocity measurements impose hard lower limits on achievable probe volumes. Potential effects of the probe volume and RWF should be taken into account, particularly in areas with large velocity gradients and spatial scales similar to those of the probe.

The observational comparison of independent, concurrent retrievals by the two DLR demonstrates the impacts of differing lidar configurations and underscores the variation that can arise in the measured wakes. The intercomparison of the instruments roughly coincides with expectations from the virtual instruments and builds confidence in the ability of the model. Some of the additional variability and deviations compared to the simulations, especially in Cases 1 and 2, can likely be ascribed to the wider range of conditions and wake behaviors not reflected in the LES period. For example, the geometry shifts when the wake lofts or the vertical extent expands rather than shrinking and can produce distortion effects that may differ from the simulated ones. The bulk of the LES period is also remarkably stationary and possible transitory effects may be understated in its results.

7 Conclusions

We consider potential distortions in the measurements of a single turbine wake made by scanning lidar at the Perdigão campaign. By employing virtual scanning lidar instruments in a case study simulation, we highlight the distortions that can occur in the retrieval of turbine wakes due to the observation system and compare the behavior with observational data. We focus on RHI scans of a waked transect perpendicular to the parallel ridges at the site by two independent WindCube 200S lidars and use an offset, unwaked transect collected by a third lidar for reference to compute the wake deficit. The center, vertical extent, and deficit magnitude of the wake are extracted using Gaussian fits of the deficit profiles.

Even with a single lidar, the background, unwaked flow is generally well captured (error less than 0.1 m s^{-1} in reference region) assuming the scanning geometry constrains the beam elevation angles to less than 7° from horizontal and vertical velocities less than 3 m s^{-1} . Biases therefore arise from the measurement of the wake itself, particular to the lidar scanning configuration.

Our findings emphasize the overall effectiveness of lidar for wake observations, even with a relatively simple scan configuration. The measurements do largely capture the wake structure over its 4-5 D extent. Compared with the background flow, however, the lidar system responds more strongly to the scales of the wake and introduces larger errors that can systemically affect the measured behavior of the wake. This analysis suggests where biases may be present and how they arise.

The wake distortion can be largely understood as smoothing effects on the wind field due to sampling resolution and probe-volume averaging. The lidar-retrieved wake dampens the extreme velocity deficits, prematurely loses the distinction of the near wake double lobes, and can blur the wake bounds and extent. For this configuration, both lidars persistently underestimate the maximum velocity deficit by factor of 0.7–0.8. The lidar on the downwind ridge (DLR2) inflates the vertical extent of the

wake by a factor of about 1.2; the valley-based lidar (DLR1) is typically more accurate error (<10 m). Both lidar systems most accurately capture the trajectory of the wake center, maintaining errors of typically less than 5 m.

The findings using the virtual LES are reinforced by the observational data. Inter-comparison of DLR1 and DLR2 wake metrics display similar behavior using real and virtual lidar data, suggesting that the model is able to capture how the systems
460 measure the wake and the resulting differences between the two configurations.

The decomposition of the lidar system into stages, enabled by the model, provides insight that can inform potential improvements to scanning strategies. For the Perdigão case, the limitation of the beam elevation angles around the wake prove largely effective at minimizing error due to contamination by projected vertical velocities. Instead, the limited spatial resolution emerges as a leading cause of wake measurement error. We recommend scanning configurations that increase the density of
465 retrieval points over the wake by reducing the spacing between range gates and placement or angular resolution to reduce the distance between beams; the performance of DLR1 compared to DLR2 evidences some of the potential benefits. This virtual lidar tool can help enable quantification of possible errors due to scanning geometries and scanning strategies, to enable optimal field experiment planning and instrument deployment.

Code and data availability. The WRF MMC source code is available from https://github.com/a2e-mmc/WRF/tree/mmc_update_v4.3. Virtual lidar code may be found at <https://gitlab.com/raro0632/virtual-lidar>. Observational lidar data are available as part of the Perdigão campaign database at <https://doi.org/10.17616/R31NJMN4> (note that the lidar designated by DLR2 was swapped on 3 June 19:20 UTC from instrument number 85 to 89 in the archive). The namelist used for the simulation, the virtual lidar data collected from the LES, and corresponding fitted deficit profiles analyzed here are archived at <https://doi.org/10.5281/zenodo.10652098>.
470

Appendix A: Double Gaussian wake characteristics

475 Illustration of the behavior of the double Gaussian functions fit to the deficit profiles (Eq. 10, Fig. A1). Representing the properties of maximum deficit and the vertical extent of the wake cannot always be done as a simple, closed-form function of the input parameters (a , σ , z_{sep}). When the two Gaussian lobes overlap more closely, z_{sep} becomes smaller relative to the widths of the individual Gaussian lobes, σ , they add in a more complex way.

To be consistent with the single Gaussian properties and to accurately reflect the physical behavior we care about, we directly
480 estimate the maximum value of g_2 and where it decays to 5 % of its maximum to determine the amplitude and width. These estimates are done with evaluation of the function at many points rather than a direct calculation with the input parameters.

The transition from near to far wake is determined by the double Gaussian fit. The merging of the individual lobes is reflected in a smaller separation relative to the width of each lobe so that they are no longer distinct. An empirically picked threshold of $z_{sep} = 2w$ is used as a cutoff (Figure A1(a)).

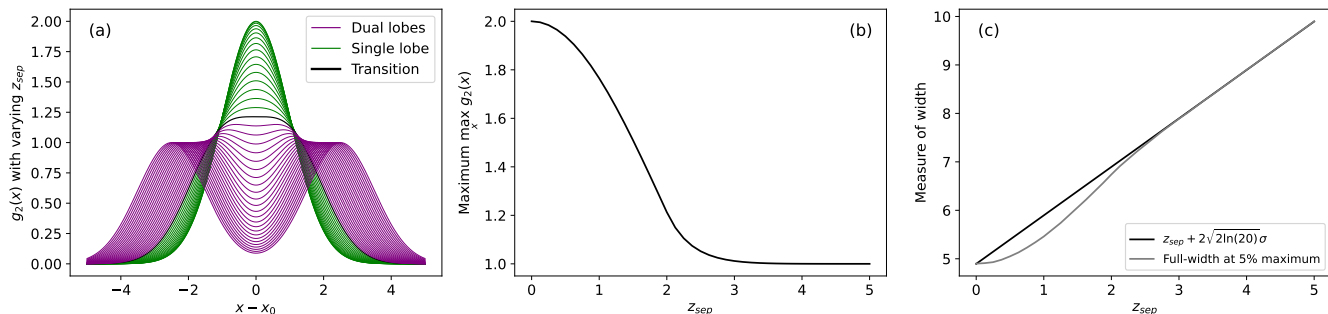


Figure A1. (a) Double Gaussian curves, $g_2(x)$, with varying z_{sep} and fixed amplitude $a = 1$ and width $\sigma = 1$ showing the transition of classification of from near (purple) to far (green) wake fits using an empirically picked threshold of $z_{sep} = 2\sigma$ (black). The corresponding (b) maximum and (c) width of the double Gaussian as a function of z_{sep} .

485 *Author contributions.* **Rachel Robey:** methodology, software, analysis and investigation, writing and editing. **Julie K. Lundquist:** conceptualization, methodology, writing and editing.

Competing interests. At least one of the (co-)authors is a member of the editorial board of Wind Energy Science.

Disclaimer. This work was authored in part by the National Renewable Energy Laboratory, operated by Alliance for Sustainable Energy, LLC, for the U.S. Department of Energy (DOE) under Contract No. DE-AC36-08GO28308. Funding provided by the U.S. Department of Energy Office of Energy Efficiency and Renewable Energy Wind Energy Technologies Office. The views expressed in the article do not necessarily represent the views of the DOE or the U.S. Government. The U.S. Government retains and the publisher, by accepting the article for publication, acknowledges that the U.S. Government retains a nonexclusive paid-up, irrevocable, worldwide license to publish or reproduce the published form of this work, or allow others to do so, for U.S. Government purposes.

495 *Acknowledgements.* Thanks to Adam Wise, who did the original Perdigão simulations in WRF, for his help matching his configuration and making the necessary updates to run with WRF 4.3. Thanks to Nathan Agarwal for processing and filtering tower data for identification and characterization of conditions for case studies within the field campaign.

This material is based upon work supported by the U.S. Department of Energy, Office of Science, Office of Advanced Scientific Computing Research, Department of Energy Computational Science Graduate Fellowship under Award Number DE-SC0021110.

This research has been supported by the US National Science Foundation (grant no. AGS-1565498).

500 We would like to acknowledge high-performance-computing support from Cheyenne (doi:10.5065/D6RX99HX) provided by National Center for Atmospheric Research's Computational and Information Systems Laboratory, sponsored by the National Science Foundation.

References

- Aitken, M. L. and Lundquist, J. K.: Utility-Scale Wind Turbine Wake Characterization Using Nacelle-Based Long-Range Scanning Lidar, *Journal of Atmospheric and Oceanic Technology*, 31, 1529–1539, <https://doi.org/10.1175/JTECH-D-13-00218.1>, 2014.
- 505 Aitken, M. L., Rhodes, M. E., and Lundquist, J. K.: Performance of a Wind-Profiling Lidar in the Region of Wind Turbine Rotor Disks, *Journal of Atmospheric and Oceanic Technology*, 29, 347–355, <https://doi.org/10.1175/JTECH-D-11-00033.1>, 2012.
- Aitken, M. L., Banta, R. M., Pichugina, Y. L., and Lundquist, J. K.: Quantifying Wind Turbine Wake Characteristics from Scanning Remote Sensor Data, *Journal of Atmospheric and Oceanic Technology*, 31, 765–787, <https://doi.org/10.1175/JTECH-D-13-00104.1>, 2014.
- Amidror, I.: Scattered Data Interpolation Methods for Electronic Imaging Systems: A Survey, *Journal of Electronic Imaging*, 11, <https://doi.org/10.1117/1.1455013>, 2002.
- 510 Arthur, R. S., Mirocha, J. D., Marjanovic, N., Hirth, B. D., Schroeder, J. L., Wharton, S., and Chow, F. K.: Multi-Scale Simulation of Wind Farm Performance during a Frontal Passage, *Atmosphere*, 11, 245, <https://doi.org/10.3390/atmos11030245>, 2020.
- Banakh, V. A. and Smalikho, I. N.: Estimation of the Turbulence Energy Dissipation Rate from the Pulsed Doppler Lidar Data, *Journal of Atmospheric and Oceanic Optics*, 10, 957–965, 1997.
- 515 Barthelmie, R. J. and Pryor, S. C.: Automated Wind Turbine Wake Characterization in Complex Terrain, *Atmospheric Measurement Techniques*, 12, 3463–3484, <https://doi.org/10.5194/amt-12-3463-2019>, 2019.
- Bodini, N., Zardi, D., and Lundquist, J. K.: Three-Dimensional Structure of Wind Turbine Wakes as Measured by Scanning Lidar, *Atmospheric Measurement Techniques*, 10, 2881–2896, <https://doi.org/10.5194/amt-10-2881-2017>, 2017.
- Boquet, M., Royer, P., Cariou, J.-P., Machta, M., and Valla, M.: Simulation of Doppler Lidar Measurement Range and Data Availability, *Journal of Atmospheric and Oceanic Technology*, 33, 977–987, <https://doi.org/10.1175/JTECH-D-15-0057.1>, 2016.
- 520 Bossard, M., Feranec, J., and Otahel, J.: CORINE Land Cover Technical Guide: Addendum 2000, Technical Report 40, European Environment Agency, 2000.
- Brugger, P., Debnath, M., Scholbrock, A., Fleming, P., Moriarty, P., Simley, E., Jager, D., Roadman, J., Murphy, M., Zong, H., and Porté-Agel, F.: Lidar measurements of yawed-wind-turbine wakes: characterization and validation of analytical models, *Wind Energy Science*, 5, 1253–1272, <https://doi.org/10.5194/wes-5-1253-2020>, 2020.
- 525 Cariou, J.-P. and Boquet, M.: LEOSPHERE Pulsed Lidar Principles, in: UpWind WP6 on Remote Sensing Devices, pp. 1–32, Orsay, France, 2010.
- Doubrawa, P., Barthelmie, R. J., Wang, H., Pryor, S. C., and Churchfield, M. J.: Wind Turbine Wake Characterization from Temporally Disjunct 3-D Measurements, *Remote Sensing*, 8, 939, <https://doi.org/10.3390/rs8110939>, 2016.
- 530 Farr, T. G., Rosen, P. A., Caro, E., Crippen, R., Duren, R., Hensley, S., Kobrick, M., Paller, M., Rodriguez, E., Roth, L., Seal, D., Shaffer, S., Shimada, J., Umland, J., Werner, M., Oskin, M., Burbank, D., and Alsdorf, D.: The Shuttle Radar Topography Mission, *Reviews of Geophysics*, 45, <https://doi.org/10.1029/2005RG000183>, 2007.
- Fernando, H. J. S., Mann, J., Palma, J. M. L. M., Lundquist, J. K., Barthelmie, R. J., Belo-Pereira, M., Brown, W. O. J., Chow, F. K., Gerz, T., Hocut, C. M., Klein, P. M., Leo, L. S., Matos, J. C., Oncley, S. P., Pryor, S. C., Bariteau, L., Bell, T. M., Bodini, N., Carney, M. B.,
535 Courtney, M. S., Creegan, E. D., Dimitrova, R., Gomes, S., Hagen, M., Hyde, J. O., Kigle, S., Krishnamurthy, R., Lopes, J. C., Mazzaro, L., Neher, J. M. T., Menke, R., Murphy, P., Oswald, L., Otarola-Bustos, S., Pattantyus, A. K., Rodrigues, C. V., Schady, A., Sirin, N., Spuler, S., Svensson, E., Tomaszewski, J., Turner, D. D., van Veen, L., Vasiljević, N., Vassallo, D., Voss, S., Wildmann, N., and Wang,

- Y.: The Perdigoão: Peering into Microscale Details of Mountain Winds, *Bulletin of the American Meteorological Society*, 100, 799–819, <https://doi.org/10.1175/BAMS-D-17-0227.1>, 2019.
- 540 Gottschall, J.: Wake Measurements with Lidar, in: *Handbook of Wind Energy Aerodynamics*, edited by Stoevesandt, B., Schepers, G., Fuglsang, P., and Yuping, S., pp. 1–18, Springer International Publishing, Cham, https://doi.org/10.1007/978-3-030-05455-7_55-1, 2020.
- Haupt, S. E., Kosovic, B., Shaw, W., Berg, L. K., Churchfield, M., Cline, J., Draxl, C., Ennis, B., Koo, E., Kotamarthi, R., Mazzaro, L., Mirocha, J., Moriarty, P., Muñoz-Esparza, D., Quon, E., Rai, R. K., Robinson, M., and Sever, G.: On Bridging A Modeling Scale Gap: Mesoscale to Microscale Coupling for Wind Energy, *Bulletin of the American Meteorological Society*, 100, 2533–2550, <https://doi.org/10.1175/BAMS-D-18-0033.1>, 2019.
- 545 Haupt, S. E., Kosović, B., Berg, L. K., Kaul, C. M., Churchfield, M., Mirocha, J., Allaerts, D., Brummet, T., Davis, S., DeCastro, A., Dettling, S., Draxl, C., Gagne, D. J., Hawbecker, P., Jha, P., Juliano, T., Lassman, W., Quon, E., Rai, R. K., Robinson, M., Shaw, W., and Thedin, R.: Lessons Learned in Coupling Atmospheric Models across Scales for Onshore and Offshore Wind Energy, *Wind Energy Science*, 8, 1251–1275, <https://doi.org/10.5194/wes-8-1251-2023>, 2023.
- 550 Iungo, G. and Porté-Agel, F.: Measurement Procedures for Characterization of Wind Turbine Wakes with Scanning Doppler Wind LiDARs, *Advances in Science and Research*, 10, 71–75, <https://doi.org/10.5194/asr-10-71-2013>, 2013.
- Iungo, G. V., Wu, Y.-T., and Porté-Agel, F.: Field Measurements of Wind Turbine Wakes with Lidars, *Journal of Atmospheric and Oceanic Technology*, 30, 274–287, <https://doi.org/10.1175/JTECH-D-12-00051.1>, 2013.
- Käsler, Y., Rahm, S., Simmet, R., and Kühn, M.: Wake Measurements of a Multi-MW Wind Turbine with Coherent Long-Range Pulsed Doppler Wind Lidar, *Journal of Atmospheric and Oceanic Technology*, 27, 1529–1532, <https://doi.org/10.1175/2010JTECHA1483.1>, 2010.
- 555 Mann, J.: DTU WS3 Scanning Lidar Data, <https://doi.org/10.17616/R31NJMN4>, available at <https://perdigao.fe.up.pt/datasets/thredds/catalog/upperAir/Lidar/DTU%20Scanning%20Lidar%20Data/netcdf/transect/WS3/catalog.>, 2019.
- Martínez-Tossas, L. A., Churchfield, M. J., and Leonardi, S.: Large eddy simulations of the flow past wind turbines: actuator line and disk modeling, *Wind Energy*, 18, 1047–1060, <https://doi.org/10.1002/we.1747>, <https://onlinelibrary.wiley.com/doi/pdf/10.1002/we.1747>, 2015.
- 560 Menke, R., Vasiljević, N., Hansen, K. S., Hahmann, A. N., and Mann, J.: Does the Wind Turbine Wake Follow the Topography? A Multi-Lidar Study in Complex Terrain, *Wind Energy Science*, 3, 681–691, <https://doi.org/10.5194/wes-3-681-2018>, 2018.
- Menke, R., Vasiljević, N., Mann, J., and Lundquist, J. K.: Characterization of Flow Recirculation Zones at the Perdigoão Site Using Multi-Lidar Measurements, *Atmospheric Chemistry and Physics*, 19, 2713–2723, <https://doi.org/10.5194/acp-19-2713-2019>, 2019.
- 565 Meyer Forsting, A., Troldborg, N., and Borraccino, A.: Modelling Lidar Volume-Averaging and Its Significance to Wind Turbine Wake Measurements, *Journal of Physics: Conference Series*, 854, 012 014, <https://doi.org/10.1088/1742-6596/854/1/012014>, 2017.
- Mirocha, J. D., Kosovic, B., Aitken, M. L., and Lundquist, J. K.: Implementation of a Generalized Actuator Disk Wind Turbine Model into the Weather Research and Forecasting Model for Large-Eddy Simulation Applications, *Journal of Renewable and Sustainable Energy*, 6, 013 104, <https://doi.org/10.1063/1.4861061>, 2014.
- 570 Moriarty, P., Hamilton, N., Debnath, M., Herges, T., Isom, B., Lundquist, J. K., Maniaci, D., Naughton, B., Pauly, R., Roadman, J., and Shaw, W.: American WAKE Experiment (AWAKEN) (NREL/TP-5000-75789), Tech. Rep. NREL/TP-5000-75789, National Renewable Energy Lab.(NREL), Golden, CO (United States), 2020.
- National Centers for Environmental Prediction, National Weather Service, NOAA, U.S. Department of Commerce: NCEP GFS 0.25 Degree Global Forecast Grids Historical Archive, 2015.
- 575

- Newsom, R., Calhoun, R., Ligon, D., and Allwine, J.: Linearly Organized Turbulence Structures Observed Over a Suburban Area by Dual-Doppler Lidar, *Boundary-Layer Meteorology*, 127, 111–130, <https://doi.org/10.1007/s10546-007-9243-0>, 2008.
- Porté-Agel, F., Bastankhah, M., and Shamsoddin, S.: Wind-Turbine and Wind-Farm Flows: A Review, *Boundary-Layer Meteorology*, 174, 1–59, <https://doi.org/10.1007/s10546-019-00473-0>, 2020.
- 580 Robey, R. and Lundquist, J. K.: Behavior and Mechanisms of Doppler Wind Lidar Error in Varying Stability Regimes, *Atmospheric Measurement Techniques*, 15, 4585–4622, <https://doi.org/10.5194/amt-15-4585-2022>, 2022.
- Rodrigo, J. S., Cantero, E., García, B., Borbón, F., Irigoyen, U., Lozano, S., Fernande, P. M., and Chávez, R. A.: Atmospheric Stability Assessment for the Characterization of Offshore Wind Conditions, *Journal of Physics: Conference Series*, 625, 012044, <https://doi.org/10.1088/1742-6596/625/1/012044>, 2015.
- 585 Rösner, B., Egli, S., Thies, B., Beyer, T., Callies, D., Pauscher, L., and Bendix, J.: Fog and Low Stratus Obstruction of Wind Lidar Observations in Germany—A Remote Sensing-Based Data Set for Wind Energy Planning, *Energies*, 13, 3859, <https://doi.org/10.3390/en13153859>, 2020.
- Skamarock, W. C., Klemp, J. B., Dudhia, J., Gill, D. O., Liu, Z., Berner, J., Wang, W., Powers, J. G., Duda, M. G., Barker, D. M., and Huang, X.-Y.: A Description of the Advanced Research WRF Model Version 4, Tech. rep., UCAR/NCAR, <https://doi.org/10.5065/1DFH-6P97>, 2019.
- 590 Smalikho, I. N., Banakh, V. A., Pichugina, Y. L., Brewer, W. A., Banta, R. M., Lundquist, J. K., and Kelley, N. D.: Lidar Investigation of Atmosphere Effect on a Wind Turbine Wake, *Journal of Atmospheric and Oceanic Technology*, 30, 2554–2570, <https://doi.org/10.1175/JTECH-D-12-00108.1>, 2013.
- Sorbjan, Z. and Grachev, A. A.: An Evaluation of the Flux–Gradient Relationship in the Stable Boundary Layer, *Boundary-Layer Meteorology*, 135, 385–405, <https://doi.org/10.1007/s10546-010-9482-3>, 2010.
- 595 Spitznagel, E. L.: 6 Logistic Regression, in: *Handbook of Statistics*, edited by Rao, C. R., Miller, J. P., and Rao, D. C., vol. 27 of *Epidemiology and Medical Statistics*, pp. 187–209, Elsevier, [https://doi.org/10.1016/S0169-7161\(07\)27006-3](https://doi.org/10.1016/S0169-7161(07)27006-3), 2007.
- Vasiljević, N., Lea, G., Courtney, M., Cariou, J.-P., Mann, J., and Mikkelsen, T.: Long-Range WindScanner System, *Remote Sensing*, 8, 896, <https://doi.org/10.3390/rs8110896>, 2016.
- 600 Vasiljević, N., L. M. Palma, J. M., Angelou, N., Carlos Matos, J., Menke, R., Lea, G., Mann, J., Courtney, M., Frölen Ribeiro, L., and M. G. C. Gomes, V. M.: Perdigoão 2015: Methodology for Atmospheric Multi-Doppler Lidar Experiments, *Atmospheric Measurement Techniques*, 10, 3463–3483, <https://doi.org/10.5194/amt-10-3463-2017>, 2017.
- Virtanen, P., Gommers, R., Oliphant, T. E., Haberland, M., Reddy, T., Cournapeau, D., Burovski, E., Peterson, P., Weckesser, W., Bright, J., van der Walt, S. J., Brett, M., Wilson, J., Millman, K. J., Mayorov, N., Nelson, A. R. J., Jones, E., Kern, R., Larson, E., Carey, C. J., Polat, 605 Í., Feng, Y., Moore, E. W., VanderPlas, J., Laxalde, D., Perktold, J., Cimrman, R., Henriksen, I., Quintero, E. A., Harris, C. R., Archibald, A. M., Ribeiro, A. H., Pedregosa, F., van Mulbregt, P., and SciPy 1.0 Contributors: SciPy 1.0: Fundamental Algorithms for Scientific Computing in Python, *Nature Methods*, 17, 261–272, <https://doi.org/10.1038/s41592-019-0686-2>, 2020.
- Wildmann, N.: DLR Scanning Lidar Data, <https://doi.org/10.17616/R31NJMN4>, available at <https://perdigao.fe.up.pt/datasets/thredds/catalog/upperAir/Lidar/DLR%20Scanning%20Lidar%20Data/catalog.>, 2019.
- 610 Wildmann, N., Kigle, S., and Gerz, T.: Coplanar Lidar Measurement of a Single Wind Energy Converter Wake in Distinct Atmospheric Stability Regimes at the Perdigoão 2017 Experiment, *Journal of Physics: Conference Series*, 1037, 052006, <https://doi.org/10.1088/1742-6596/1037/5/052006>, 2018a.

- Wildmann, N., Vasiljevic, N., and Gerz, T.: Wind Turbine Wake Measurements with Automatically Adjusting Scanning Trajectories in a Multi-Doppler Lidar Setup, *Atmospheric Measurement Techniques*, 11, 3801–3814, <https://doi.org/10.5194/amt-11-3801-2018>, 2018b.
- 615 Wise, A. S., Neher, J. M. T., Arthur, R. S., Mirocha, J. D., Lundquist, J. K., and Chow, F. K.: Meso- to Microscale Modeling of Atmospheric Stability Effects on Wind Turbine Wake Behavior in Complex Terrain, *Wind Energy Science*, 7, 367–386, <https://doi.org/10.5194/wes-7-367-2022>, 2022.